Title: Estimating the Probability of Cellular Arrhythmias with Simplified Statistical Models that Account for Experimentally Observed Uncertainty in Underlying Biophysical Mechanisms.

Qingchu Jin[1], Joseph L. Greenstein[1], Raimond L. Winslow[1*]

[1]Department of Biomedical Engineering, Johns Hopkins University, MD 21218, USA

*To whom correspondence may be addressed.

Email: rwinslow@jhu.edu

Abstract

Early afterdepolarizations (EADs) and ectopic beats (EBs) are cellular arrhythmias that can trigger cardiac arrhythmias. Simulations using biophysically-detailed cardiac myocyte models can reveal how cellular properties influence the probability of cellular arrhythmias, however such analyses often pose a huge computational burden. Here, we develop a simplified approach in which logistic regression models (LRMs) are used to define a mapping between cellular properties and the probability of cellular arrhythmias. Two LRMs are developed, one for predicting the probability of EADs (P(EAD)) as a function of I_{Ks} parameters and one for predicting the probability of EBs (P(EB)) as a function of Ca^{2+} dynamics, ryanodine receptor opening rate, and I_{K1} current density. These LRMs, which require negligible computational resources, are then used to demonstrate how uncertainties in experimentally measured model parameters influence P(EAD) and P(EB). We refer to this as arrhythmia sensitivity analysis. In the investigation of five different I_{Ks} parameters associated with Long QT syndrome 1 (LQTS1) mutations, the predicted P(EAD), when rank ordered for 6 LQTS1 mutations, matches the trend in risk from patients with the same mutations as measured by clinical cardiac event rates. We also demonstrate the degree to which parameter uncertainties map to uncertainty of P(EAD), with I_{Ks} conductance having the greatest impact. In the analysis of P(EB), as $[Ca^{2+}]_{SR}$ uncertainty is increased, P(EB) uncertainty first increases, changing from a sharp unimodal distribution to a broad uniform distribution, and then decreases towards a bimodal distribution with peaks at P(EB) values of 0 and 1.

Keywords

Cardiac electrophysiology, myocyte computational modeling, model simplification, early afterdepolarization, delayed afterdepolarization induced ectopic beat, Long QT syndrome, uncertainty analysis

Introduction

Early and delayed after-depolarizations (EADs and DADs, respectively) are forms of cellular arrhythmias that can trigger cardiac arrhythmias (1-4). EADs are depolarizations that occur during the plateau or rapid repolarization phase of action potentials (APs). DADs are spontaneous depolarizations that occur during diastole. When their amplitude is sufficiently large, DADs can trigger APs known as ectopic beats (EBs) (5). These cellular arrhythmias can trigger large scale cardiac arrhythmias in the setting of long QT syndrome (e.g. EADs) and catecholaminergic polymorphic ventricular tachycardia (e.g. DADs) (1-4). Computational modeling of these cellular arrhythmias has provided insights into the mechanisms by which they can trigger arrhythmias in the heart (6-9).

We seek to understand how variations in the underlying biophysical properties or physiological state of the myocyte influence the probability of occurrence of these cellular arrhythmias. We refer to this as arrhythmia sensitivity analysis. To do this, we use a three-dimensional model of the ventricular myocyte developed by Walker et al (10) in which the fundamental events governing intracellular Ca^{2+} dynamics are modeled stochastically. The advantage of using this model is that it reproduces realistic Ca^{2+} waves and DADs driven by stochastic gating of L-type Ca^{2+} channels and Ca^{2+} release channels (ryanodine receptors, RyRs). This model was used previously to study mechanisms of DAD variability and to estimate P(DAD) through direct, repeated simulations. Here we explore an alternative approach designed for estimating the probability of DAD-induced EBs that is more computationally efficient than methods described previously by Walker et al (10). To do this we leverage techniques first developed

by Sobie et al (11, 12) to formulate a logistic regression model (LRM) that maps myocyte model inputs (MMIs), which refers collectively to myocyte model parameters as well as state variable initial and boundary conditions, to probabilities of cellular arrhythmias. Using this approach, we demonstrate how uncertainty in experimental estimates of MMIs influences our ability to reliably estimate the probability of EADs and EBs, denoted P(EAD) and P(EB), respectively.

Ventricular myocyte function in disease is studied experimentally by identifying the biological sub-systems whose function is perturbed in disease, and then characterizing the impact of these perturbations. Computational models of myocyte function in disease are formulated by using experimental data to estimate how parameters of myocyte sub-systems are altered in disease. Understanding the molecular basis of cellular arrhythmias in disease therefore requires an understanding of how changes in myocyte model parameters impact the probability of occurrence of EAD and DAD events that lead to cellular arrhythmias. Action potential duration (APD) prolongation and QT-interval prolongation have been widely used as surrogates for increased arrhythmogenic potential (13-16). However, the relationship between these surrogate features and the likelihood of arrhythmia is indirect. For example, ranolazine leads to QT prolongation (surrogate proarrhythmic indicator) in multiple clinical trials (17, 18), however, it in fact has been shown to have anti-arrhythmic effects (19). Rather than relying upon indirect indicators of arrhythmic potential, in this work we develop model-based methods for estimating the probability of occurrence of the actual cellular arrhythmic events of interest. Furthermore, this approach allows for evaluation of the relationship between these event probabilities and their associated MMIs.

Diastolic cytosolic Ca^{2+} concentration ($[Ca^{2+}]_i$), sarcoplasmic reticulum (SR) Ca^{2+} load ($[Ca^{2+}]_{SR}$), conductance of the inward rectifier current I_{K1} (G_{K1}), and ryanodine receptor (RyR) opening rate (k_{RyR^+}) were selected as MMIs to parameterize the LRM for P(EB). In their myocyte model, Walker et. al. previously demonstrated that elevated $[Ca^{2+}]_i$ or $[Ca^{2+}]_{SR}$, as well as downregulation of I_{K1} increased P(EB) (10). Paavola et. al. showed the positive correlation of k_{RyR^+} with DAD induction (20). Down-regulation of I_{K1} has been shown experimentally to be associated with ventricular arrhythmias in conditions such as Anderson's syndrome (21) and Long QT Syndrome (22). Down-regulation of I_{K1} (23) and an increase in k_{RyR^+} (24) have both been demonstrated in failing cardiac myocytes. Five slow potassium current (I_{Ks})-related biophysical parameters were chosen as MMIs to parameterize the LRM for P(EAD). Mikuni et. al. demonstrated with a human myocyte model that loss-of-function of I_{Ks} leads to the occurrence of EADs (25). Long QT Syndrome type 1 (LQTS1) arises from mutations in the alpha subunit KCNQ1 of I_{Ks} (26). Jons et. al. described electrophysiological changes associated with 17 LQTS1 mutations by identifying the altered values of these same five I_{Ks}-related parameters for each mutation (8).

Use of a LRM to map MMIs to the probability of cellular arrhythmias also enables analysis of how experimental uncertainty in MMIs influences estimates of these probabilities. One mainstream method for experimental uncertainty analysis is Monte Carlo (27) which has been used in system biology and myocyte modeling (28-30). However, such methods require many repeated model simulations, which can become intractable when using a complex three-dimensional stochastic model of the myocyte such as that of Walker et. al. (10) LRMs provide a computationally efficient approach for performing uncertainty analyses. This study presents the following three uncertainty analyses in the context of cellular arrhythmias: 1) the impact of $[Ca^{2+}]_{SR}$ uncertainty on predicted P(EB), 2) the impact of uncertainty in the degree of heart failure-related downregulation of I_{K1} on P(EB), and 3) the impact of uncertainty in LQTS1 related I_{Ks} parameters on P(EAD).

In this study, we develop a LRM-based computationally efficient approach for estimating the probability of cellular arrhythmia events as a function of underlying biophysical properties of the myocyte. Using these LRMs, the impact of uncertainty in experimentally based MMIs on the probabilities of cellular arrhythmia events is evaluated.

Two LRMs are developed, one mapping 5 MMIs (I_{Ks}-related parameters) to P(EAD) and one mapping 4 MMIs (I_{K1} conductance (G_{K1}), RyR opening rate (k_{RyR^+}), $[Ca^{2+}]_i$ and $[Ca^{2+}]_{SR}$) to P(EB). In the investigation of 5 different I_{Ks} parameters functionally associated with LQTS1 mutations, the trend in predicted P(EAD), when rank ordered for 6 LQTS1 mutations, matches the trend in risk from patients with the same mutations as measured by clinical 30-year cardiac event rates. We also demonstrate the degree to which uncertainty in each parameter maps to

uncertainty of P(EAD) with I_{Ks} conductance having the greatest impact. Investigation of the role of uncertainty in $[Ca^{2+}]_{SR}$ on P(EB) surprisingly reveals that as $[Ca^{2+}]_{SR}$ uncertainty increases, P(EB) uncertainty first increases (from a sharp unimodal distribution to a broad uniform-like distribution) and then decreases (toward a bimodal distribution with P(EB) concentrated at 0 or 1). Investigation of I_{K1} uncertainty showed that P(EB), with I_{K1} density at levels associated with heart failure, is statistically significantly higher than that at normal I_{K1} density. These results demonstrate the potential for arrhythmia risk prediction using model-based approaches for estimation of P(EB) and P(EAD).

Results

Modeling Ectopic Beat Probability. Fig. 1A shows 5 examples each of myocyte model (MM)-simulated DAD-induced EBs and DADs. Since EBs consistently exhibit membrane potential waveforms that exceed 0 mV whereas DADs do not, a threshold of 0 mV was used to detect such events in each realization (Fig. 1A). We defined a biophysically meaningful range (region of interest, ROI) of MMIs within which the LRM is built (Table 4). Fig. 1B demonstrates the relationship between MMIs within the ROI and P(EB), where $\underline{B}_f^T\underline{P}_f$ is the weighted ($\underline{B}_f$) summation of LRM features ($\underline{P}_f$ contains all MMIs and nonlinear features derived from the MMIs) that appear in the logistic regression equation (see Materials and Methods Eq. 2). This nonlinear relationship allows for identification of three domains in the ROI of MMIs: transition domain (TD), left plateau domain (LPD), and right plateau domain (RPD). The TD is a region in which P(EB) is a sensitive function of $\underline{B}_f^T\underline{P}_f$, corresponding to the steep part of the curve in Fig. 1B. The LPD and RPD are both regions where P(EB) is essentially insensitive to MMI perturbation, with P(EB)=~0 in the LPD (left flat part of the curve in Fig.1B) and P(EB)=~1 in the RPD (right flat part of the curve in Fig.1B). To build the LRM, we sampled 200 MMI sets within the ROI and ran 100 realizations for each MMI set from which we obtain P(EB). Since the TD is relatively narrow and P(EB) is a very steep function within it, i.e., strongly dependent on MMI values, we have developed a two-stage sampling strategy to ensure adequate sampling of the TD (see Materials and Methods and Supplement for details). These 200 MMI sets and their corresponding P(EB)s were used to train the LRM. The LRM enables a direct calculation of P(EB) for any MMI set without simulation of the MM. Fig. 1B and 1C demonstrates the LRM training performance. Fig. 1C shows the predicted P(EB)s from LRM versus actual P(EB)s computed from MM simulations using the training data set (200 MMI sets). The LRM performs well in predicting P(EB) (R^2 = 0.981 for the 102 MMI sets inside the TD, mean prediction error (see Materials and Methods Eq. 3) = 0.021 ± 0.034), despite the highly complex nonlinear properties of the MM. Fig. 1B-C demonstrates that the LRM achieves good performance on the training set. To test generalizability of the LRM, Fig. 1D and 1E compare the LRM predicted P(EB)s to actual MM-generated P(EB)s using test data consisting of 100 independent MMI sets. The LRM also performs well on the test set (R^2 = 0.993 for the 22 MMI sets within the TD, mean prediction error = 0.006 ± 0.013). This model performance indicates that the predicted P(EB) for MMIs within the specified ROI will on average differ by no more than 0.006 from the actual P(EB) of the underlying myocyte model. Detailed modeling methods and performance metrics are described in Materials and Methods.

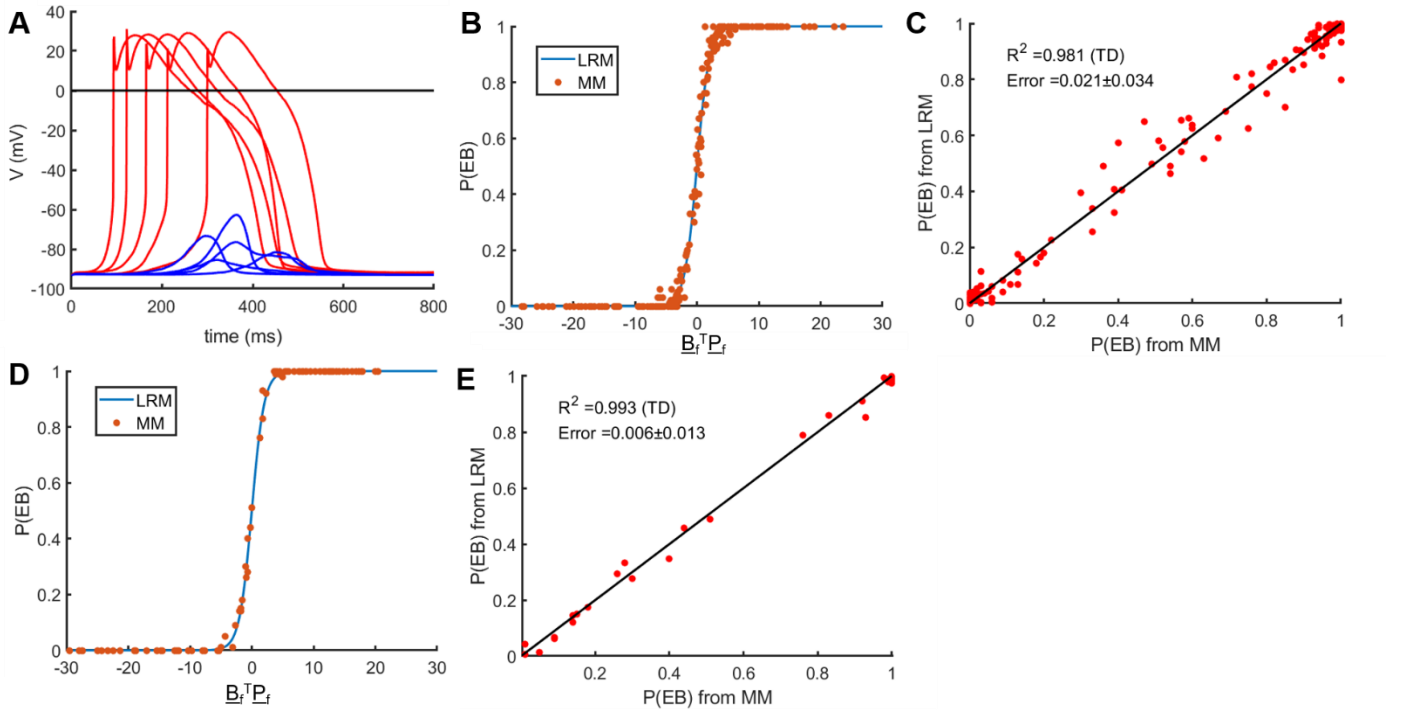

Fig. 1. DAD-induced ectopic beat study. (A) Simulations of triggered DAD-induced EBs (red) and simulations that generate DADs without induced EBs (blue). (B) Comparison between LRM-predicted P(EB)s (blue) and MM-generated actual P(EB)s (red) as a function of $\underline{B}_f^T\underline{P}_f$, the term in the logistic equation (Eq. 2 for the training set). (C) Direct comparison between LRM-predicted P(EB)s (y-axis) and MM-generated actual P(EB)s (x-axis) for the training set. (D) and (E) show the same analyses described in (B) and (C), respectively, for the independent test set. R^2 is calculated only from MMI sets within the TD, LRM: logistic regression model, MM: myocyte model

The LRM for P(EB) was formulated with a total of 10 features. Four of these are linear features: $[Ca^{2+}]_i$, $[Ca^{2+}]_{SR}$, G_{K1} scaling factor (G_{k1}_sf), and k_{RyR}^+ scaling factor (k_{RyR}^+_sf). In addition, the following 6 derived quadratic features were used: $[Ca^{2+}]_{SR}^2$, $[Ca^{2+}]_{SR}$*k_{RyR}^+_sf, k_{RyR}^+_sf^2, G_{K1}_sf^2, $[Ca^{2+}]_i^2$, and G_{K1}_sf*k_{RyR}^+_sf. Prior to fitting the LRM, features were scaled to a range of 0 to 1 in order to ensure interpretability of the LRM weights. Table 1 shows the LRM weights ranked by feature importance. Feature $[Ca^{2+}]_{SR}$ is most important and is followed by feature k_{RyR}^+. $[Ca^{2+}]_{SR}^2$ ranks as the third most important feature, indicating that quadratic features play an important role in improving model performance. In Fig. S1B, the performance of the LRM built without quadratic features on the same test set has lower R^2 (0.862) in the TD and higher error (0.023 ± 0.058) than the 10-feature model shown in Fig. 1C. This confirms that the additional 6 quadratic features improve LRM performance. Fig. 2A-D demonstrate the relationship between P(EB) and each MMI. In Fig. 2A-D, with the exception of the MMI that is varied along the x-axis, MMIs were fixed at the following values: $[Ca^{2+}]_i$ = 150 nM, $[Ca^{2+}]_{SR}$ = 0.5 mM, k_{RyR}^+_sf = 5 and G_{K1}_sf = 0.338. Results show that elevated $[Ca^{2+}]_i$ and $[Ca^{2+}]_{SR}$ increase P(EB). I_{K1} downregulation also increases P(EB). These findings agree with earlier simulations by Walker et. al. (10). The positive correlation between k_{RyR}^+_sf and P(EB) agrees with the finding of Paavola et. al that k_{RyR}^+ is positively related to DAD induction (20). Fig. 2E and 2F show multiple MM realizations for two example MMI sets. Fig. 2E is an example with relatively low P(EB) obtained using the MMI set: $[Ca^{2+}]_i$ = 216 nM, $[Ca^{2+}]_{SR}$ = 0.47 mM, G_{K1}_sf = 0.699, and k_{RyR}^+_sf = 5.60, where 19 out of 100 simulations generated EBs. Fig. 2F is an example with relatively high P(EB) obtained using the MMI set: $[Ca^{2+}]_i$ =154 nM, $[Ca^{2+}]_{SR}$=0.60 mM, G_{K1}_sf = 0.775, and k_{RyR}^+_sf = 5.13, where 92 out 100 simulations generated EBs. The only difference across simulations in either Fig. 2E or 2F is the random gating of RyRs and L-type Ca^{2+} channels.

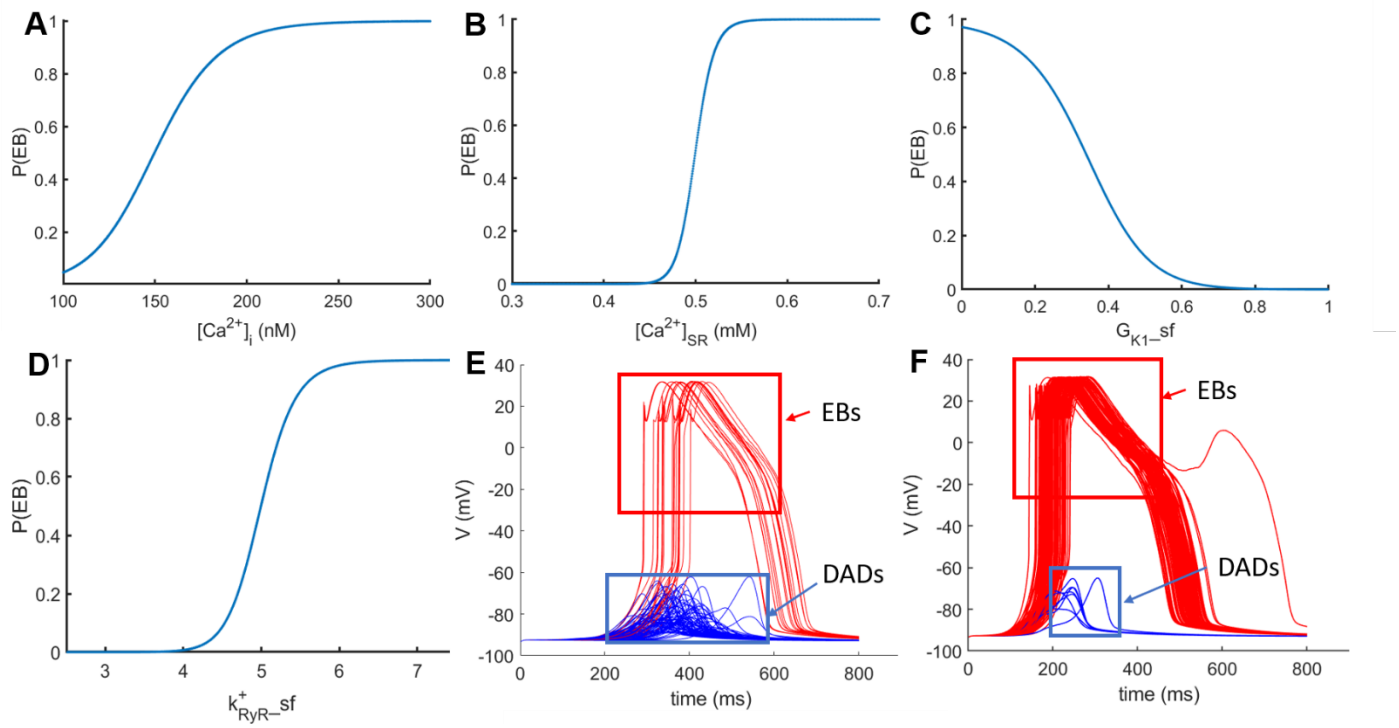

Fig. 2 Relationship between MMIs and P(EB). In A-D, with exception of the MMI that is varied along the x-axis, MMIs are fixed at: $[Ca^{2+}]_i$ =150 nM, $[Ca^{2+}]_{SR}$ = 0.5 mM, G_{K1}_sf = 0.338, and k_{RyR}^+_sf = 5. (E) 100 random myocyte model simulations with a low P(EB) = 0.19 MMI set: $[Ca^{2+}]_i$ = 216 nM, $[Ca^{2+}]_{SR}$ = 0.47 mM, G_{K1}_sf = 0.699, and k_{RyR}^+_sf = 5.60. (F) 100 random myocyte model simulations with a high P(EB) = 0.92 MMI set: $[Ca^{2+}]_i$ =154 nM, $[Ca^{2+}]_{SR}$ = 0.60 mM, G_{K1}_sf = 0.775, and k_{RyR}^+_sf = 5.13. Red curves represent EBs and blue curves represent DADs that do not trigger EBs.

Table 1. DAD-induced EB features ranked by relative importance

Ranking	Features	Weights ± SE from LRM
1	$[Ca^{2+}]_{SR}$	71.27 ± 3.81
2	k_{RyR}^+_sf	44.37 ± 2.56
3	$[Ca^{2+}]_{SR}{}^2$	-24.41 ± 2.13
4	$[Ca^{2+}]_{SR}$*k_{RyR}^+_sf	-15.36 ± 2.76
5	k_{RyR}^+_sf^2	-13.45 ± 1.14
6	$[Ca^{2+}]_i$	12.77 ± 0.53
7	G_{K1}_sf	-7.98 ± 0.62
8	G_{K1}_sf^2	-3.62 ± 0.49
9	$[Ca^{2+}]_i{}^2$	-2.68 ± 0.46
10	G_{K1}_sf*k_{RyR}^+_sf	-2.48 ± 0.54

Uncertainty analysis of P(EB). The LRM allows for analysis of the uncertainty of probabilistic events such as EBs arising from the experimental uncertainties inherent in measurements of the MMIs. We treat MMIs as random variables (RVs), and then P(EB), which is a function (i.e. Eq. 2) of these MMIs, also becomes a RV. MMIs with uncertainties are assumed to have a normal distribution with σ taking the experimentally measured value for each MMI. From the experimentally derived distribution for each MMI, we randomly generate 10^6 MMI sets and evaluate the LRM for each set to generate a predicted distribution of P(EB).

In the following study, the effect of $[Ca^{2+}]_{SR}$ uncertainty on P(EB) was determined. In Fig.3A-C, MMI set 1 was assumed to represent mean values for each MMI: $[Ca^{2+}]_i$ = 150nM, $[Ca^{2+}]_{SR}$ = 500μM, k_{RyR}^+_sf = 5, and G_{K1}_sf = 0.338, which yields P(EB) = 0.5. We assumed three different degrees of uncertainty in $[Ca^{2+}]_{SR}$ corresponding to σ values of 5 μM, 15 μM, and 30 μM. In Fig. 3A-C, histograms show the P(EB) distribution given different $[Ca^{2+}]_{SR}$

uncertainties, which leads to 3 different distribution patterns: unimodal (Fig. 3A), approximately uniform (Fig. 3B), and bimodal (Fig. 3C). The red line indicates the mean P(EB). Fig. 3A (σ = 5 μM) is a unimodal distribution in which P(EB) takes on values at or near 0.5 with high probability. Fig. 3B (σ = 15 μM) is an approximately uniform distribution between 0 and 1. Thus, in this case the value of P(EB) is essentially unpredictable for any particular cell. In Fig. 3C (σ = 30 μM), the distribution of P(EB) becomes bimodal, with two peaks located at P(EB) values close to 0 and 1. In this scenario, P(EB) is equally likely to be either 0 or 1 given the symmetry of the P(EB) distribution.

In Fig. 3D, blue curves show the $[Ca^{2+}]_{SR}$-P(EB) relationship determined by the LRM, which we refer to as the model characteristic (MC) curve for $[Ca^{2+}]_{SR}$, and the red curves show $[Ca^{2+}]_{SR}$ probability density functions ($[Ca^{2+}]_{SR}$ PDF) which widen as σ increases. A comparison of the relative positions of the MC curve and the $[Ca^{2+}]_{SR}$ PDF can be used to explain the previously described P(EB) distribution patterns. The MC curve for MMI set 1 (stars) shows the $[Ca^{2+}]_{SR}$-P(EB) relationship as $[Ca^{2+}]_{SR}$ is varied. The width of the $[Ca^{2+}]_{SR}$ PDF for σ = 5 μM (solid curve) is quite narrow and exists at the center of the TD where P(EB) = 0.5. As a result, the distribution of P(EB) is unimodal with peak near 0.5. The width of the $[Ca^{2+}]_{SR}$ PDF for σ = 15 μM (dashed curve) coincides with the boundaries of the TD such that the distribution of P(EB) in Fig. 3B is approximately uniform. The $[Ca^{2+}]_{SR}$ PDF for σ = 30μM (dotted line) is much wider such that a sufficiently large portion of the $[Ca^{2+}]_{SR}$ PDF coincides with the LPD and the RPD of the MMI set 1 MC curve, where P(EB) takes on values of either 0 or 1 resulting in a bimodal distribution. This behavior reveals an interesting finding that with increasing uncertainty of $[Ca^{2+}]_{SR}$, uncertainty in P(EB) first increases and then decreases. To confirm our finding, we calculated the entropy of P(EB) distributions for Fig. 3A-C (see Supplement for details). The random variable with larger uncertainty (variance) will have a larger entropy. The P(EB) distribution with σ = 15 μM has the highest entropy which validates our finding. The mean P(EB) for all distributions shown in Fig. 3A-C is 0.5 because all variations in $[Ca^{2+}]_{SR}$ occur about a mean $[Ca^{2+}]_{SR}$ = 500 μM in this scenario.

The role of $[Ca^{2+}]_{SR}$ uncertainty on P(EB) is evaluated for two additional MMI sets for which P(EB) ≠ 0.5: MMI set 2 ($[Ca^{2+}]_i$ = 150 nM, $[Ca^{2+}]_{SR}$ = 500 μM, k_{RyR}^+_sf = 5, and G_{K1}_sf = 0.638, for which P(EB) = 0.02) and MMI set 3 ($[Ca^{2+}]_i$ = 150 nM, $[Ca^{2+}]_{SR}$ = 500 μM, k_{RyR}^+_sf = 5, and G_{K1}_sf = 0.0, for which P(EB) = 0.97). The distribution of P(EB) for MMI sets 2 and 3 are evaluated for $[Ca^{2+}]_{SR}$ uncertainty with σ = 30μM. In Fig. 3E the P(EB) distribution of $[Ca^{2+}]_{SR}$ is unimodal for both MMI set 2 and MMI set 3. MC curves for both MMI set 2 (open squares) and 3 (open circles) are shown in Fig 3D. For MMI set 2, the $[Ca^{2+}]_{SR}$ PDF (σ = 30 μM) coincides with the LPD and part of the TD of the MC curve. This results in a P(EB) distribution that is a unimodal with P(EB) values close to 0. For MMI set 3, the MC curve is shifted such that the $[Ca^{2+}]_{SR}$ PDF (σ = 30 μM) coincides with the RPD and part of the TD of the MC curve. This results in a P(EB) distribution that is a unimodal with P(EB) values close to 1. These demonstrate that the P(EB) distribution pattern depends on the width of $[Ca^{2+}]_{SR}$ PDF (degree of $[Ca^{2+}]_{SR}$ uncertainty) as well as the relative position of the mean $[Ca^{2+}]_{SR}$ with respect to the TD of its MC curve.

In general, $[Ca^{2+}]_{SR}$ uncertainty impacts the mean of P(EB). Fig. 3F shows the relationship of $[Ca^{2+}]_{SR}$ uncertainty (σ) and the mean P(EB) for MMI sets 1-3. Experimental uncertainty in measurements of $[Ca^{2+}]_{SR}$ varies widely from 10 μM to 290 μM (31-33), and we therefore evaluated 100 μM ≥ σ ≥ 0 μM. Results show that with the increase of $[Ca^{2+}]_{SR}$ uncertainty, the mean P(EB) converges to 0.5 regardless of the selected MMI set. When the $[Ca^{2+}]_{SR}$ PDF is narrow (e.g., σ = 5μM), the P(EB) distribution will be unimodal centered at the value of P(EB) defined by the LRM for the given MMI set, and therefore, the mean P(EB) will be close to this value. In contrast, when the $[Ca^{2+}]_{SR}$ uncertainty is sufficiently large, a majority of the $[Ca^{2+}]_{SR}$ PDF will coincide with the LPD and RPD of the MC curve, with only a small to negligible portion of the $[Ca^{2+}]_{SR}$ PDF coinciding with the TD of the MC curve. In the limit as σ grows to be large, for any MMI set, the distribution of $[Ca^{2+}]_{SR}$ flattens such that there is equal probability of it taking on values in either the LPD or RPD of the MC curve, and hence P(EB) becomes equally likely to take on values of 0 or 1 and mean P(EB) converges to 0.5 (Fig. 3F).

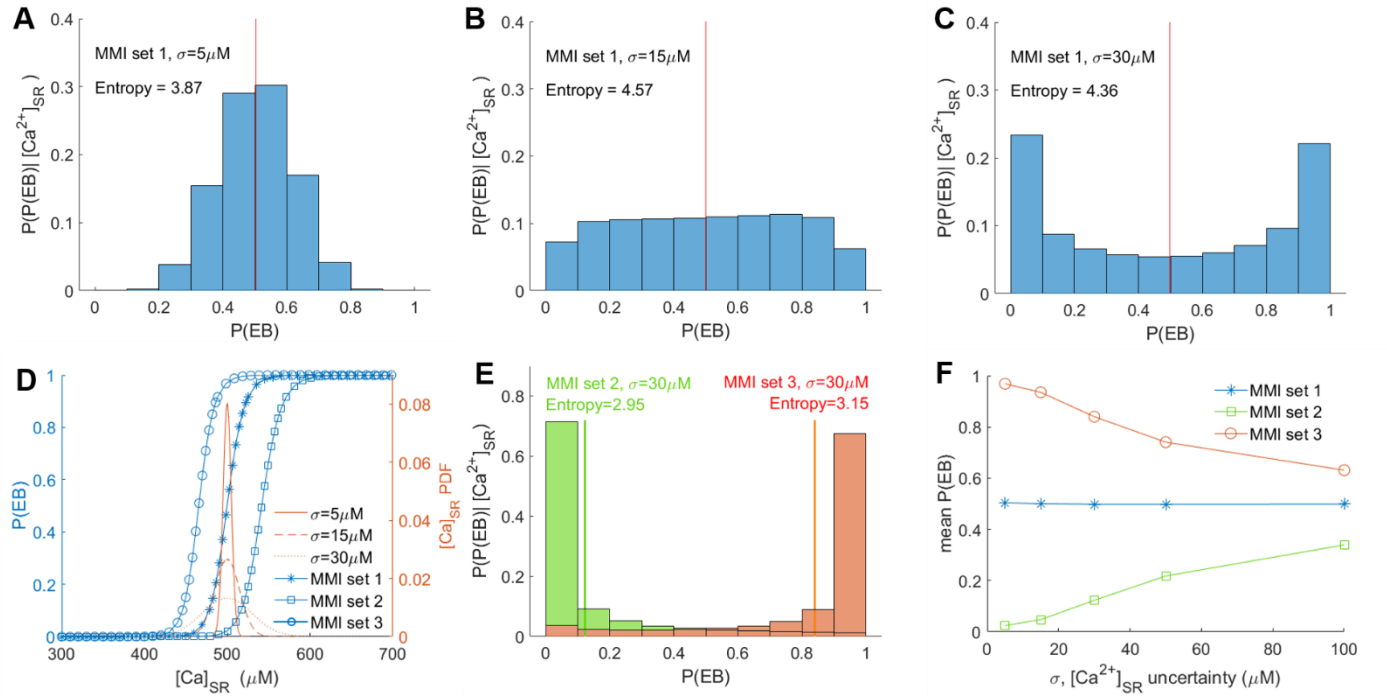

Fig. 3 Uncertainty analysis of P(EB) due to variation in $[Ca^{2+}]_{SR}$. Three MMI sets are used. All MMI sets have $[Ca^{2+}]_i$ = 150 nM, $[Ca^{2+}]_{SR}$ = 500 μM, and k_{RyR}^+_sf = 5. G_{K1}_sf for MMI set 1, MMI set 2, and MMI set 3 is 0.338, 0.638, and 0.000, respectively. The P(EB) distributions given different hypotheical $[Ca^{2+}]_{SR}$ uncertainties (σ) of MMI set 1, where (A) σ = 5 μM, (B) σ = 15 μM, and (C) σ = 30 μM. The vertical red line is the mean of the P(EB) distribution. P(P(EB)|$[Ca^{2+}]_{SR}$), on the y-axis, refers to the P(EB) distribution given $[Ca^{2+}]_{SR}$ uncertainty. (D) Red curves are the $[Ca^{2+}]_{SR}$ PDFs for σ = 5μM (solid line) , σ = 15 μM (dashed line), and σ = 30 μM (dotted line). Blue curves are the model characteristic (MC) curves relating $[Ca^{2+}]_{SR}$ and P(EB) for MMI set 1 (stars), MMI set 2 (open squares), and MMI set 3 (open circles). (E) P(EB) distributions with $[Ca^{2+}]_{SR}$ uncertainty σ = 30 μM for MMI set 2 (green bars) and MMI set 3 (red bars). (F) Relationship between mean P(EB) and $[Ca^{2+}]_{SR}$ uncertainty for all three MMI sets.

In the following study, the effect of I_{K1} current density scaling factor (G_{K1}_sf) uncertainty on P(EB) was evaluated. We used the experimental results of Pogwizd et. al. (23) to obtain the distribution of G_{K1}_sf values in both normal and heart failure myocytes. The process by which the LRM parameters (i.e. weights) are constrained is described in detail in the supplement (Fig. S4B and S4C). The following three MMIs are fixed as follows: $[Ca^{2+}]_i$ = 150 nM, $[Ca^{2+}]_{SR}$ = 550 μM, and k_{RyR}^+_sf = 5. G_{K1}_sf is treated as uncertain where in normal cells it is 1.0000 ± 0.1108 (σ_N) and in heart failure (HF) cells it is 0.5100 ± 0.0852 (σ_{HF}). The P(EB) corresponding to the mean value of G_{K1}_sf is 0.008 and 0.918 for normal and HF, respectively. Fig. 4A shows the P(EB) distributions arising from the experimental uncertainties (EUs) of G_{K1}_sf. The P(EB) arising from the experimental distribution of G_{K1}_sf is 0.0294 ± 0.0611 in normal cells and 0.8788 ± 0.1183 in HF. Results show that, even when accounting for experimental uncertainty, P(EB) for HF G_{K1}_sf is significantly higher than that corresponding to normal G_{K1}_sf. Fig. 4B shows the relative positions of the G_{K1}_sf MC curve (blue) and the G_{K1}_sf PDFs (red). The normal and HF G_{K1}_sf PDFs exhibit very little overlap. The normal G_{K1}_sf PDF primarily coincides with a region of the MC curve where P(EB) < ~0.3, with much of it in the RPD where P(EB) is near 0. In contrast, the HF G_{K1}_sf PDF primarily coincides with a region of the MC curve where P(EB) > ~0.4. The relationships between the G_{K1}_sf PDFs and the MC curve lead to the distributions of P(EB) in Fig. 4A.

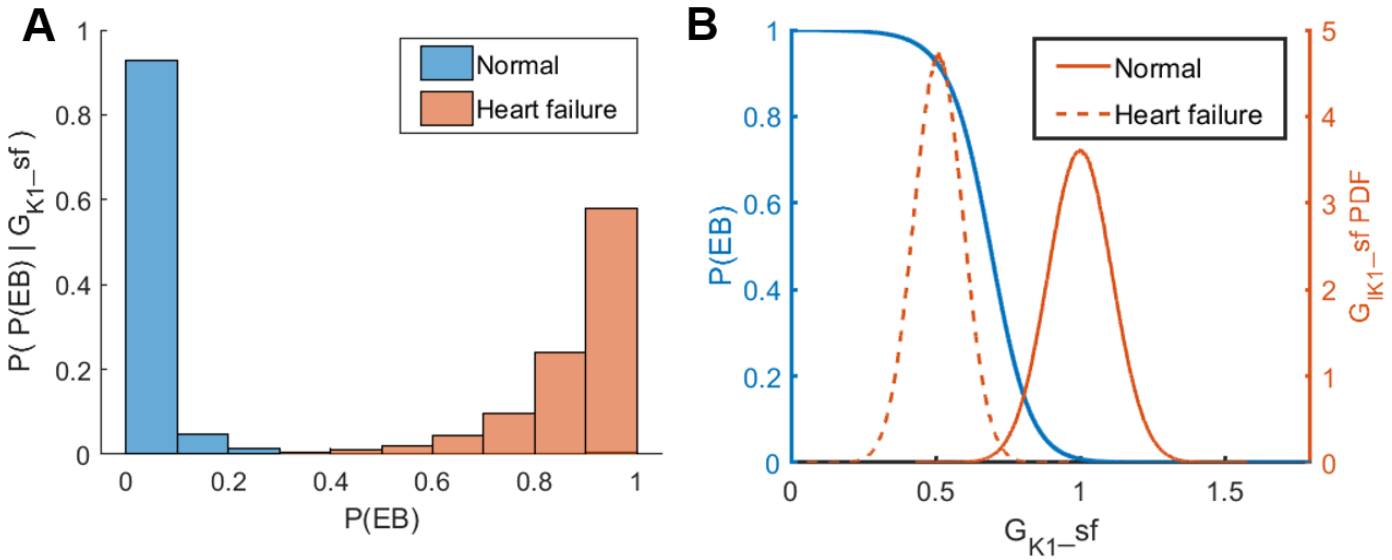

Fig. 4 Effect of G_{K1}_sf uncertainty on P(EB). (A) Distributions of P(EB) for normal G_{K1}_sf (blue) and HF G_{K1}_sf (red). (B). MC curve (blue) shows the relationship of G_{K1}_sf and P(EB) for the LRM. G_{K1}_sf PDFs for normal (solid red line) and HF (dashed red line).

Modeling the Role of I_{Ks} on Probability of EADs. Using the same process described above for modeling ectopic beat probability, an LRM was formulated to capture the quantitative relationship between P(EAD) and 5 slow K^+ current (I_{Ks})-related MMIs (activation time constant scaling factor (τ_+_sf), deactivation time constant scaling factor (τ_-_sf), shifting of half the maximal activation voltage ($\Delta V_{1/2}$), scaling factor of voltage dependence of activation curve slope (k_sf), and maximal conductance scaling factor (G_{Ks}_sf)). These 5 MMIs were chosen because these are the I_{Ks}-related biophysical properties that have been experimentally characterized for a variety of LQTS1 mutations. The LRM for P(EAD) was formulated with a total of 16 features, 5 being the linear features (τ_+_sf, τ_-_sf, $\Delta V_{1/2}$, k_sf, and G_{Ks}_sf) and 11 being quadratic features, shown in Table 2. In order to ensure interpretability of feature importance from the LRM weights, all features were scaled into a range from 0 to 1 (see Materials and Methods and Supplement for details). Fig. 5A shows examples of APs, both normal (blue) and with EADs (red). For each realization, an EAD is considered to have occurred if the membrane voltage at 500 ms following the time of stimulus current is greater than -40 mV (Fig. 5A). The panels of Fig. 5 were generated following the same procedure described for Fig. 1 applied to these 5 I_{Ks}-related MMIs. Fig. 5B and 5C compares the LRM-predicted P(EAD) to actual MM-generated P(EAD) based on 200 MMI sets that make up the training data set. The LRM achieves good performance on the training set (R^2 = 0.971 for the 96 MMI sets within the TD, mean prediction error = 0.022 ± 0.036). Fig. 5D and 5E compare the LRM-predicted P(EAD) and actual MM-generated P(EAD) using a test set consisting of 100 independent MMI sets. The LRM also performs well on the test set (R^2 = 0.933 for the 27 MMI sets within the TD, mean prediction error = 0.019 ± 0.043). Table 2 shows the LRM weights ranked by feature importance. Feature G_{Ks}_sf is the most important, and this is followed by τ_+_sf*G_{Ks}_sf, k_sf, and $\Delta V_{1/2}$*G_{Ks}_sf. The second and fourth most important features are both quadratic features, which improve LRM accuracy when compared to a LRM formulated using only the linear features as inputs (Fig. S2B, R^2 = 0.859 within TD, mean prediction error = 0.028 ± 0.063 for 100 test MMI sets).

The results presented here demonstrate that LRMs can accurately predict both P(EB) and P(EAD), the probabilities of physiologically relevant cellular arrhythmia events. For the 100 test MMI sets used in each case, thousands of CPU hours are required to obtain event probabilities from the MM whereas evaluation of LRMs requires negligible computing time on the order of milliseconds. The seemingly intractable task of estimating these probabilities in an efficient manner is made possible by this LRM approach.

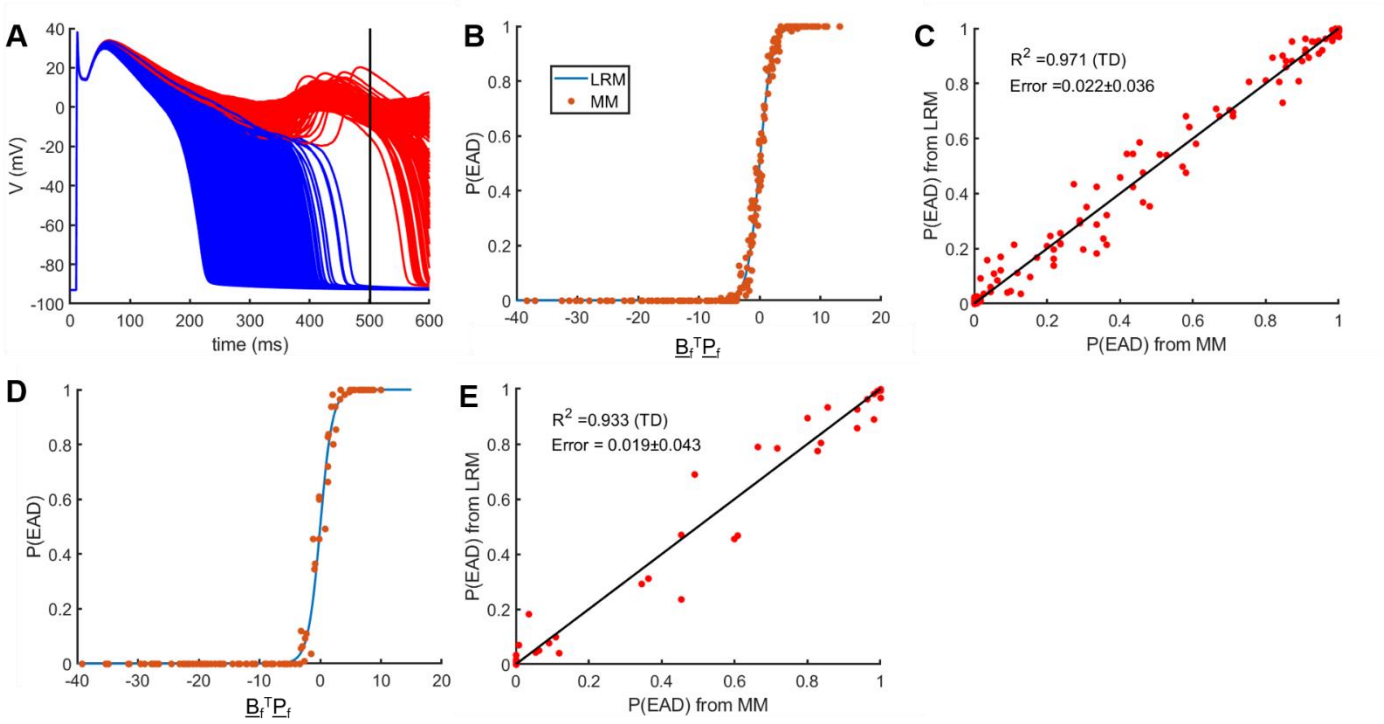

Fig. 5 EAD study. (A) Example APs from myoyte model simulations. Representative normal APs (blue) and APs with EADs (red) are shown. (B) Comparison between LRM-predicted P(EAD) (blue) and MM-generated actual P(EAD) (red) as a function of $\underline{B}_f^T\underline{P}_f$ for the training set. (C) Direct comparison between LRM-predicted P(EAD) (y-axis) and MM-generated actual P(EAD) (x-axis) for the training set. (D) and (E) show the same analyses described in (B) and (C), respectively, for the independent test set. R^2 is calculated only from MMI sets within the TD, LRM: logistic regression model, MM: myocyte model

Table 2. EAD features ranked by relative importance.

Ranking	Feature	Weight ± SE from LRM
1	G_{Ks}_sf	-63.89 ± 1.86
2	τ_+_sf * G_{Ks}_sf	34.35 ± 2.07
3	k_sf	14.57 ± 0.65
4	$\Delta V_{1/2}$ * G_{Ks}_sf	12.83 ± 1.61
5	τ_+_sf	11.90 ± 0.59
6	τ_+_sf ^{2}	-10.27 ± 0.73
7	τ_-_sf * G_{Ks}_sf	8.54 ± 1.11
8	k_sf ^{2}	-7.67 ± 0.41
9	k_sf * $\Delta V_{1/2}$	-6.31 ± 0.43
10	$\Delta V_{1/2}$	-6.05 ± 0.51
11	τ_-_sf ^{2}	-5.29 ± 0.36
12	τ_+_sf * $\Delta V_{1/2}$	-4.66 ± 0.69
13	G_{Ks}_sf * k_sf	-4.00 ±1.11
14	τ_-_sf	3.09 ± 0.62
15	k_sf * τ_-_sf	2.07 ± 0.37
16	τ_-_sf * $\Delta V_{1/2}$	-1.26 ± 0.37

Effect of LQTS1 Mutations on EAD Probability. LQTS1 arises from mutations in KCNQ1, the alpha subunit of the I_{Ks} channel (26). The symptoms of LQTS1 include syncope, cardiac arrest, and sudden death (34). Jons et al. experimentally characterized the electrophysiological properties of I_{Ks} expressed in Xenopus oocytes for 17 LQTS1 mutations and reported the 30-year cardiac event rate for each mutation (8). The 30-year cardiac event

rate is defined as the percentage of people within a population of carrier of the mutant gene, who experienced syncope, cardiac arrest, or sudden death in the first 30 years of life. For each mutation, 5 I_{Ks}-related functional parameters were measured experimentally (8). For each mutation, measurements were obtained from no less than 16 oocytes, and experimental uncertainty (EU) of each parameter was estimated using standard error (SE). Detailed experiment and clinical data are summarized in Table S1. In this study, we evaluate the 1) effect of experimental uncertainty of the estimated I_{Ks} parameters on P(EAD) and 2) use a previously built LRM formulation for P(EAD) to predict the severity of LQTS1 mutations.

The uncertainty of the 5 MMIs (i.e. the 5 I_{Ks}-related parameters) arising from the variability across the population of cells, for each mutation, is taken as the standard deviation (SD) of the reported experimental estimates, as calculated from the SE (Table S1). It is assumed that the 5 MMIs are independent normally distributed RVs, but with distributions truncated to ensure biophysically meaningful values (e.g. G_{Ks} must be nonnegative). The mean (μ) and SD (σ) of each MMI is set to be the experimental sample mean and sample SD, respectively. Uncertainty analysis is then performed with the Monte Carlo method (see details in Materials and Methods).

Fig. 6A-E show the distributions of predicted P(EAD) for mutations Y315C, W305S, G168R, T312I, and L266P which are all bimodal (similar to that for P(EB) described in Fig. 3C). This indicates that the EUs for these 5 mutations are relatively large. Fig. 6F shows the distribution of predicted P(EAD) for G314S is unimodal with high probability that P(EAD) is ~1. Distributions of P(EAD) are estimated from 10^6 feature (MMI) sets sampled from distributions based on mutation-specific EUs. Based on the uncertainty of P(EAD) across all mutations, it is clear that P(EAD) will take on values close to 0 or 1 in a large majority of cells ($P(0.1<P(EAD)<0.9) = 0.31 \pm 0.07$ across 6 mutations). The results of Fig. 6A-F also demonstrate that due to the underlying experimental uncertainties, the continuous distribution of P(EAD) can be approximated by a Bernoulli RV with parameter p, where $p = P(P(EAD) >0.5)$ for any particular MMI set (i.e. cell) and $1-p = P(P(EAD) <0.5)$. Namely, MMI sets (or model cells) can be classified as belonging to one of two subgroups, one that almost always exhibits EADs and one that almost never exhibits EADs. The parameter p, the approximate probability a cell exhibits EADs, increases gradually in the following mutation order: Y315C, W305S, G168R, T312I, L266P, and G314S.

Mean P(EAD), calculated from the P(EAD) distribution for each mutation in Fig. 6A-F, is shown by the red vertical line. In Fig. 6G, mean P(EAD)s for each mutation are compared with the 30-year cardiac event rate reported by Jons et al (8). The correlation of predicted P(EAD) and cardiac event rate demonstrate that the LRM-predicted P(EAD) may be a useful indicator of the mutation-specific risk of clinical arrhythmias in patients. To validate the use of the LRM in uncertainty analyses, we performed Monte Carlo simulations of the MM with 200 randomly generated sample MMI sets for the L266P mutation (200 realizations were run for each MMI set). Fig. 6H shows that the distribution of P(EAD) generated from the MM faithfully matches that calculated from the LRM. The total computation time required for all MM simulations was ~17,000 CPU hours whereas the LRM model required only less than 1 CPU second.

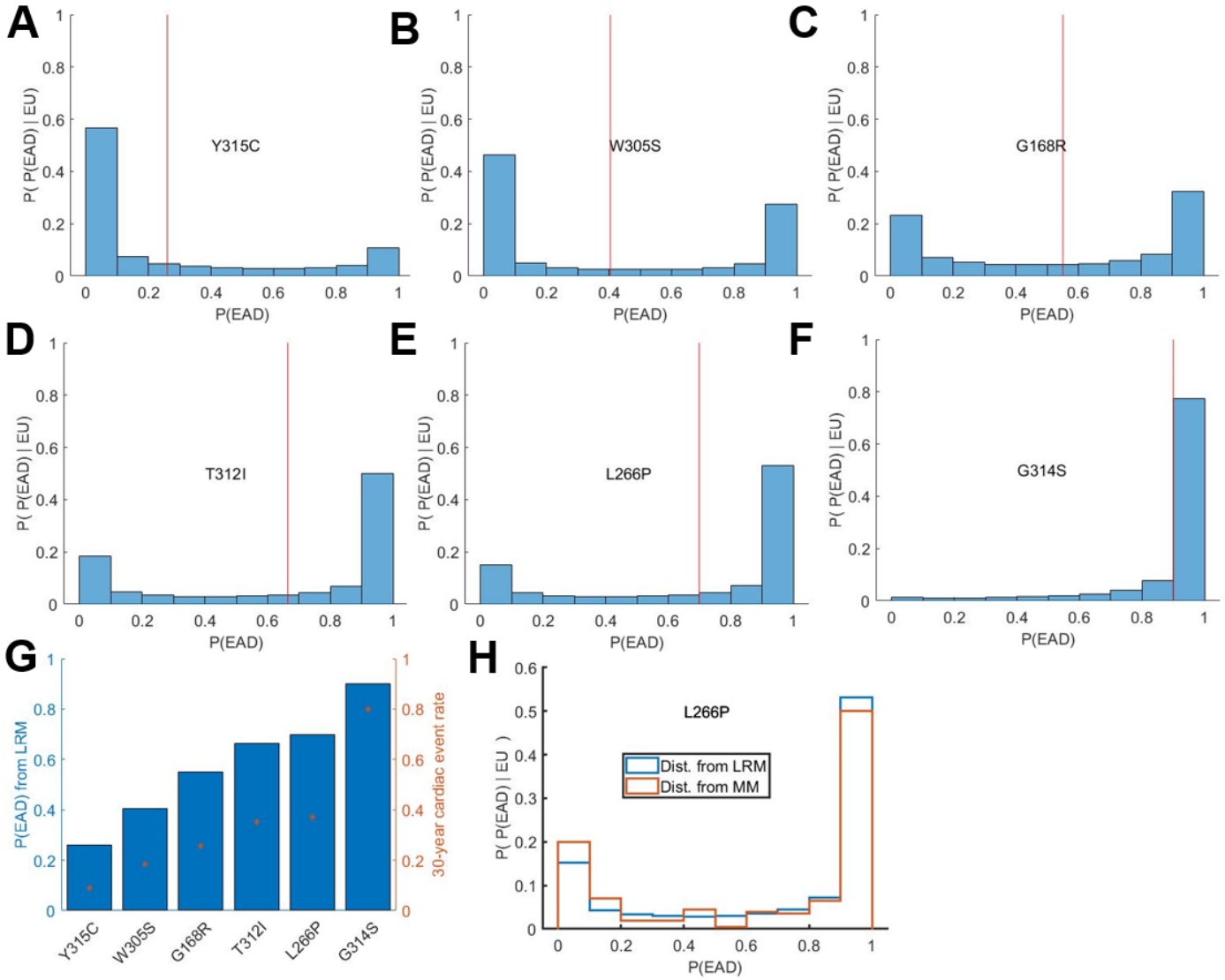

Fig. 6. LQTS1 study. LRM-based estimates of P(EAD) distribution for mutations: (A) Y315C, (B) W305S, (C) G168R, (D) T312I, (E) L266P, and (F) G314S. Red vertical lines in A-F represent the mean P(EAD) of each mutation. P(P(EAD)|EU) on the y-axis, refers to the P(EAD) distribution given mutation-specific experimental uncertainties. (G) Mean P(EAD) of each mutation versus the corresponding 30-year cardiac event rate (8). (H) Comparison of P(EAD) distributions for L266P computed using the LRM (blue) and MM (red).

To further delineate the effects of EU in the measured properties of I_{Ks} for each mutation, we evaluated the contribution of each individual MMI to the uncertainty of P(EAD) separately for all mutations. To do this, for each mutation, only a single MMI (i.e. a single member of the MMI set which consists of τ_+_sf, τ_-_sf, $\Delta V_{1/2}$, k_sf, and G_{Ks}_sf) is allowed to vary while all others are assigned a constant value equal to their experimentally measured mean value, and this process is repeated for each MMI in the set. Recall that $\underline{B}_f^T\underline{P}_f$ is a function of the MMIs which appears in the logistic regression equation. In order to compare the impact of individual MMI EUs on P(EAD) across all MMIs (rather than for only a single MMI as in Figs. 3D and 4B), the PDF of $\underline{B}_f^T\underline{P}_f$ (red) is compared to the MC curve plotted as a function of $\underline{B}_f^T\underline{P}_f$ (blue) in Fig. 7A-F. Here, $\underline{B}_f^T\underline{P}_f$ is the weighted summation of 16 I_{Ks} features and the MC curve (blue) relates $\underline{B}_f^T\underline{P}_f$ to P(EAD). In Fig. 7A, $\underline{B}_f^T\underline{P}_f$ PDFs are shown for each mutation arising from variations in τ_+_sf based on its EU with all other MMIs held constant. Figs. 7B-E show the same analyses for τ_-_sf, $\Delta V_{1/2}$, k_sf, and G_{Ks}_sf. In Fig. 7F, all five MMIs vary simultaneously based on their EUs simulating the mutation-specific distribution of I_{Ks} properties observed experimentally. In Fig. 7B and D, the widths of the $\underline{B}_f^T\underline{P}_f$ PDFs are quite narrow, indicating that variability in τ_-_sf and k_sf have relatively small impact on P(EAD). In Fig. 7A and C, the widths of the $\underline{B}_f^T\underline{P}_f$ PDFs are wider and span a significant portion of the TD for many of the mutations indicating that uncertainty in τ_+_sf and $\Delta V_{1/2}$ have a greater influence on predicted P(EAD). The uncertainty in P(EAD), however, is most heavily influenced by the EU of G_{Ks}_sf as shown in Fig. 7E where

most mutations exhibit $\underline{B}_f^T\underline{P}_f$ PDFs that are sufficiently wide to encompass the entire TD as well as large portions of the LPD and RPD (where the exception is G314S which coincides with the TD and RPD only, consistent with the unimodal distribution of Fig. 6F). This means that the EU in G_{Ks} spans across values that result in cells that never exhibit EADs to those that exhibit EADs on every beat. Note that the $\underline{B}_f^T\underline{P}_f$ PDFs in Fig. 7F, where all MMIs vary simultaneously, are nearly identical to those of Fig. 7E, indicating that G_{Ks} uncertainty is the dominant player determining uncertainty in P(EAD) for all mutations.

$\underline{B}_f^T\underline{P}_f$ PDFs for each mutation are quantitatively compared in Table 3, based on their mean (μ) and SD (σ). For each mutation, regardless of which MMI is allowed to vary, μ is always close the μ_{all} (μ of the $\underline{B}_f^T\underline{P}_f$ PDF where all 5 MMIs vary based on their EUs). We rank the contribution of MMIs to P(EAD) uncertainty by computing the average ratio between σ where only one MMI is allowed to vary and σ_{all} where all 5 MMIs are allowed to vary across all mutations. G_{Ks}_sf ($\sigma_{GKs_sf}/\sigma_{all}$ = 0.95 ± 0.03) contributes most, then followed by τ_+_sf ($\sigma_{\tau+_sf}/\sigma_{all}$ = 0.23 ± 0.05), $\Delta V_{1/2}$ ($\sigma_{\Delta V1/2}/\sigma_{all}$ = 0.17 ± 0.06), k_sf ($\sigma_{k_sf}/\sigma_{all}$ = 0.06 ± 0.05), and τ_-_sf ($\sigma_{\tau-_sf}/\sigma_{all}$ = 0.03 ± 0.01). The finding that $\sigma_{GKs_sf}/\sigma_{all}$ = ~1 is consistent with Fig. 7E indicating that G_{Ks} uncertainty is the dominant player determining uncertainty in P(EAD) for all mutations.

In Fig. 7F, a comparison of relative positions of the MC curve of $\underline{B}_f^T\underline{P}_f$ and $\underline{B}_f^T\underline{P}_f$ PDFs can be used to explain P(EAD) distribution patterns shown in Fig 6. For mutation G314S, the $\underline{B}_f^T\underline{P}_f$ PDF (squares) coincides with RPD and part of the TD of the MC curve. This results in a P(EAD) distribution that is unimodal close to 1. For the other 5 mutations, $\underline{B}_f^T\underline{P}_f$ PDFs all coincodes with LPD and RPD of the MC curve, thus resulting in a P(EAD) distribution that is bimodal.

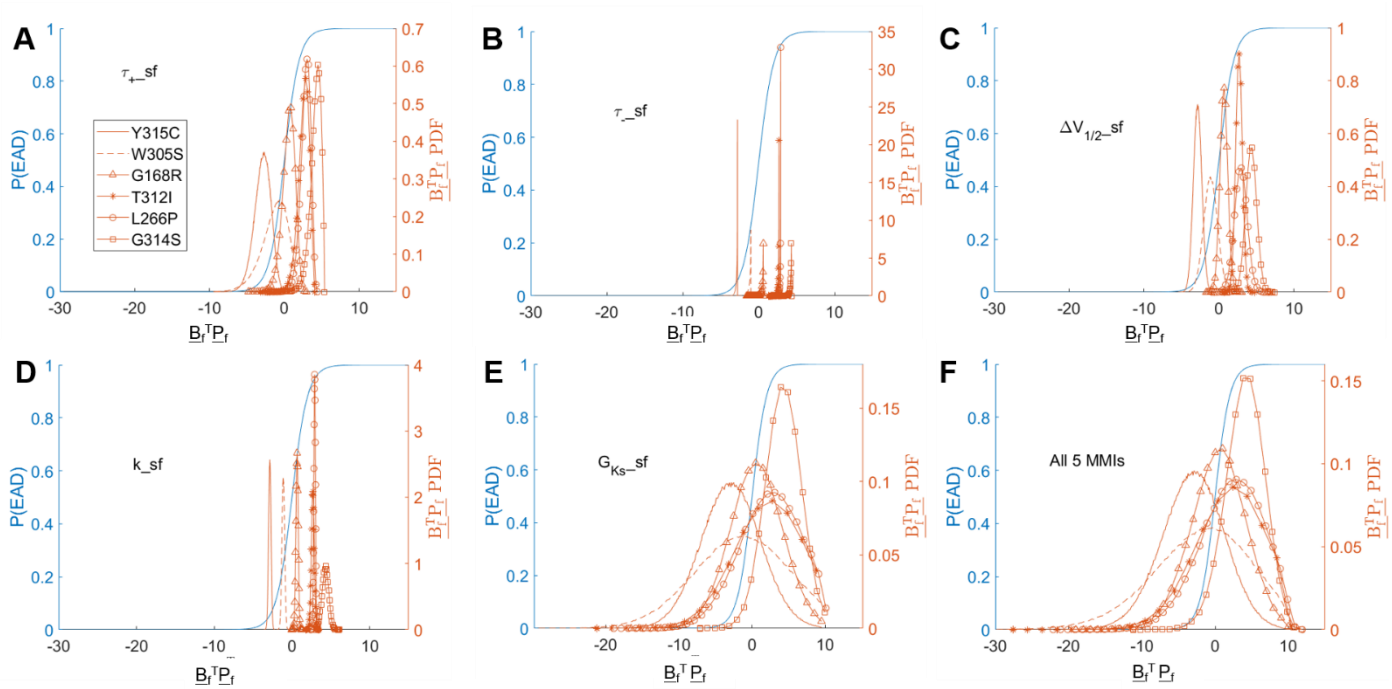

Fig. 7 Uncertainty analysis for individual features underlying LQTS1 mutations. $\underline{B}_f^T\underline{P}_f$ PDFs (red) are shown for each mutation (Y315C: solid line, W305S: dashed line, G168R: triangle markers, T312I: star markers, L266P: circle markers, and G314S: square markers). $\underline{B}_f^T\underline{P}_f$ is the weighted summation of 16 I_{Ks} features (5 MMIs + 11 MMI-derived quadratic features) for each mutation. The MC curve (blue) relates $\underline{B}_f^T\underline{P}_f$ to P(EAD). Single feature uncertainties: (A) τ_+_sf, (B) τ_-_sf, (C) $\Delta V_{1/2}$, (D) k_sf, or (E) G_{Ks}_sf are sampled from an experimentally based distribution while other MMIs are assumed fixed at their mean. (F) All five MMIs in the set are sampled to calculate the $\underline{B}_f^T\underline{P}_f$ PDFs that reflect combined uncertainty of all features in the MMI set.

Table 3. Mean (μ) and standard deviation (σ) of $\underline{B}_f^T\underline{P}_f$ PDFs. Only the indicated MMI is allowed to vary.

	τ_+_sf		τ_-_sf		$\Delta V_{1/2}$	
	$\mu_{\tau+_sf}$	$\sigma_{\tau+_sf}$	$\mu_{\tau-_sf}$	$\sigma_{\tau-_sf}$	$\mu_{\Delta V1/2}$	$\sigma_{\Delta V1/2}$
Y315C	-2.921	1.104	-2.903	0.138	-2.851	0.564

W305S	-1.354	1.744	-1.203	0.220	-1.119	0.923
G168R	0.585	0.834	0.564	0.133	0.657	0.516
T312I	2.583	0.741	2.633	0.075	2.679	0.438
L266P	2.844	0.664	2.863	0.078	2.918	0.847
G314S	4.195	0.712	4.262	0.100	4.305	0.714
	k_sf		G_{Ks}_sf		all 5 MMIs	
	μ_{k_sf}	σ_{k_sf}	μ_{GKs_sf}	σ_{GKs_sf}	μ_{all}	σ_{all}
Y315C	-2.853	0.158	-2.863	4.023	-2.987	4.221
W305S	-1.121	0.175	-1.791	6.058	-2.106	6.449
G168R	0.656	0.151	0.613	3.519	0.444	3.669
T312I	2.676	0.190	1.984	4.338	1.840	4.450
L266P	2.916	0.103	2.380	4.057	2.246	4.224
G314S	4.301	0.415	4.245	2.343	4.090	2.604

Discussion

Regression models have been used previously by Sobie et al. to estimate action potential duration, peak and resting membrane potential, and Ca^{2+} transient amplitude from deterministic myocyte models, as well as the probability of the occurrence of Ca^{2+} sparks from a stochastic Ca^{2+} release site model (11, 12). Based on their method, we developed a new pipeline for establishing simplified models (LRMs) for estimating the probability of cellular cardiac arrhythmia events simulated by a complex stochastic myocyte model. Fig. 1 and Fig. 5 show good prediction performance of the LRMs in predicting the probability of both EBs and EADs. The method developed in this work is universal in the sense that it can be considered a general approach to simplifying highly complex nonlinear stochastic models in a wide range of applications.

Our approach differs from that of Lee at al. (12) at two points in the modeling pipeline. First, we developed a two-iteration MMI set generation strategy. The first iteration randomly samples MMI sets within the ROI uniformly. The second iteration randomly samples additional MMI sets only from within the transition domain (TD). This method ensures that the TD is sampled at a higher frequency than the plateau domain (PD), which improves LRM performance. Second, we derived LRM quadratic features from the MMIs. The rationale for this approach is that since the MM is highly nonlinear, we expect improved performance by allowing for a nonlinear relationship between MMIs and P(event) in the LRM, where “event” refers to an EB, an EAD, or any other probabilistic outcome of interest. Incorporating quadratic features enables the LRM to capture nonlinear relationships between MMIs and P(event). To demonstrate the performance improvement of these two steps, for both EAD and EB studies, we built LRMs from only the first iteration MMI sets and using only MMIs as features (i.e. without derived quadratic features). For prediction of P(EB), this approach yields an average error of 0.026 ± 0.058 (Fig.S1A and S1D), which is worse than that (0.006 ± 0.013) of the LRM formulated with the full pipeline (Fig. 1). Similarly, for prediction of P(EAD), this approach yields an average error of 0.030 ± 0.059 (Fig. S2A and S2D), which is worse than that (0.019 ± 0.043) of the full pipeline (Fig. 5).

The LRM approach has the benefit of computational efficiency. The average computational time required for each MMI set in the EAD study is ~0.4 (realizations per hour) * 100 (realizations) = 40 CPU hours. The computational time required to run the test set (100 MMI sets) in the EAD study is therefore 4000 CPU hours. In contrast, the computational time for LRMs is negligible (~5 CPU ms). However, to build the LRM, 200 training MMI sets are required to run with the MM, which take ~8000 CPU hours. For the uncertainty analysis, in Fig. 6H, the L226P P(EAD) distribution using MM (200 MMI sets and 200 realizations for each set) costs ~16,000 CPU hours (C++) and the LRM costs ~0.5 CPU second (MATLAB R2018b), which again shows the dramatic computational efficiency of the LRM.

LRMs enable us to quantitatively explore the relationship between MMIs and event probabilities. In the EB study, Fig. 2A and 2B show that P(EB) increases with increasing $[Ca^{2+}]_i$ and $[Ca^{2+}]_{SR}$, indicating that elevation of cellular Ca^{2+} (i.e. Ca^{2+} overload) tends to increase the likelihood of ectopic beats. This result is consistent with previous experimental and computational studies (10, 35). Fig. 2C shows that increasing G_{K1}_sf reduces P(EB). I_{K1} downregulation has been shown to be associated with ventricular arrhythmias such as Anderson's syndrome (36) and LQTS (22). Increased k_{RyR}^+_sf is also shown in Fig. 2D to elevate P(EB). Kubalova et. al. showed that heart failure myocytes exhibit elevated RyR open probability (24). Paavola et. al. also demonstrated the positive correlation between RyR opening rate with DAD induction and Ca^{2+} waves (20). The EAD study shows that G_{Ks} is the most impactful parameter of I_{Ks} with regard to P(EAD) because in the ranking of feature importance, it is associated with the first, second, and fourth features. In Fig. 7, we also showed that, for 6 LQTS1 mutations, G_{Ks} experimental uncertainty is the dominant contributor to the P(EAD) uncertainty. Fig. S5 shows that it is negatively correlated with P(EAD). This result follows from the fact that I_{Ks} is a repolarizing current. With the decrease of conductance of I_{Ks}, the action potential becomes more prone to depolarizing events, thus leading to higher likelihood of EAD occurrence (37).

In Fig. 3A-C, in which $[Ca^{2+}]_{SR}$ variation was explored, three P(EB) distribution patterns (unimodal, approximately uniform, and bimodal) were revealed when exploring the role of $[Ca^{2+}]_{SR}$ uncertainty on predictions of P(EB). This implies that with the increase of $[Ca^{2+}]_{SR}$, the uncertainty of P(EB) first increases and then decreases. This result is also confirmed by comparing the entropies of P(EB) distributions associated with different degrees of uncertainty in $[Ca^{2+}]_{SR}$. Reported EUs (standard errors) of $[Ca^{2+}]_{SR}$ vary widely from 10μM to 290μM (31-33). A consequence of this is that for the majority of the realistic uncertainty range (30 - 290 μM), myocytes are unlikely to be in the TD where both DADs and EBs occur with nonzero probability. Namely, with a small perturbation in $[Ca^{2+}]_{SR}$ relative to the EU range, the most likely behavior of the cell would jump between always exhibiting DADs and always exhibiting EBs. This is consistent with the fact that the EB is a bifurcation phenomenon in the stochastic myocyte model. Other studies also showed that EBs arise as a result of a bifurcation (38). In Fig. 6A-E, the bimodal shape is also observed when analyzing the effect of LQTS1 mutations on P(EAD). This indicates that EAD is also a bifurcation behavior, which also has been confirmed by other studies (39, 40).

The bimodal uncertainty distribution has a specific meaning in a cell population. For a cell population, the experimental parameter uncertainty of a cell population represents the single-cell variability. It exists in the cell population, which can be caused by, but not limited to variations in gene expression (41) and metabolism (42). The bimodal distribution reveals that the cell population can be separated into two subgroups with respect to P(event), where one group has low P(event) and the other group has high P(event). It is unlikely to find individual cells that exhibit intermediate P(event) values (i.e. close to 0.5). To quantitatively delineate the portions of two subgroups, the P(EAD) distribution can be approximated by a Bernoulli RV with parameter p = P(P(EAD)>0.5). The proportion of the cell group with high P(event) is p and the proportion of the cell group with low P(event) is 1-p.

The I_{K1} uncertainty study shows that P(EB) associated with HF G_{K1} is statistically significantly higher than P(EB) of normal G_{K1}. This method can be generalized to test the pro-arrhythmia effect on other ion currents. We chose to explore G_{K1} in HF myocytes because I_{K1} data were available, and this method can be used to explore other MMIs as well.

Action potential duration (APD) and QT prolongation have been widely used as surrogates, both in basic science research and in clinical settings, as indicators of disease (13, 14) and drug-related arrhythmogenic effects (15, 16). However, there are examples which have shown the dissociation of these two surrogates with arrhythmia or arrhythmogenic effects. For example, alfuzosin prolongs APD and QT interval but is not linked to occurrence of Torsades de pointes (TdP), a polymorphic ventricular tachycardia (43). Ranolazine prolongs QT interval but has been shown to be antiarrhythmic (19). Unlike these indirect surrogates, an EAD is a fundamental cellular

arrhythmia event. The stochastic myocyte model, in principle, can be used to estimate P(EAD) but doing so is unrealistic because of its high computational burden. Such estimates become possible with our LRM. We successfully utilized P(EAD) to correctly rank the severity of 6 LQTS1 mutations out of 17 mutations (based on experiments of Jons et al. (8)) based on the severity determined by clinical outcome (Fig. 3A). Predictions failed to match clinical results for the remaining 11 mutations, potentially due to the following reasons: 1) The stochastic MM is a canine midmyocardial ventricular myocyte model, which is somewhat quantitatively distinct from human myocytes in terms of some essential ion channels properties such as Ca^{2+}-independent transient outward K^+ current (I_{to1}) (44). 2) Tissue-level networking effect is ignored. Xie et. al. used computational models to show that gap conductance is essential for EAD and DAD propagation inside the heart (45). 3) The mathematical characterization for LQTS1 mutations may be insufficient. In our study, I_{Ks} activation and deactivation processes are characterized by a single time constant whereas Eldstrom et al. used two activation time constants and three inactivation time constants to characterize four LQTS1 mutations (46). 4) The patient pool for some mutations is relatively small such that the derived ranking of clinical outcomes may be sensitive to sample bias. For seven of these mutations, the size of the patient cohort was less than 16 (8).

In Fig. 7 and Table 3, we qualitatively and quantitatively evaluated the contribution of each individual MMI to the uncertainty of P(EAD) for all six LQTS1 mutations. An average value of $\sigma_{GKs_sf}/\sigma_{all}$ = ~1 indicates that G_{Ks}_sf uncertainty alone provides enough information to approximately reconstruct the P(EAD) distribution. For each mutation, the $\underline{B}_f^T\underline{P}_f$ PDF in Fig. 7E arising from variability in G_{Ks}_sf alone nearly matches the $\underline{B}_f^T\underline{P}_f$ PDF in Fig. 7F, which serves to confirm this idea. This result indicates that for future LQTS1 study, I_{Ks} expression variability is more impactful than variations in its kinetic or voltage-dependent properties with respect to the uncertianty of P(EAD). A similar conclusion had been made in LQTS type 2 (LQTS2). Anderson et al. showed that protein trafficking (which ultimately impacts cell-surface expression), rather than gating or permeation (intrinsic functional properties of the channel), is the dominant mechanism for loss of Kv11.1 channel function in LQTS2 (47).

In summary, we developed a pipeline for building logistic regression models for the probability of cellular arrhythmias. These simplified models faithfully reproduce predictions of biophysically-detailed stochastic myocyte models with far less computational burden. As far as we know, this is the first simplified model enabling quantitative investigation of determinants of the probability of stochastic cellular cardiac events (delayed afterdepolarization, induced ectopic beat, and early afterdepolarization). Two types of LRMs were developed for early afterdepolarization occurrence probability (P(EAD)) and delayed afterdepolarization-induced ectopic beat occurrence probability (P(EB)). In the LQTS1 study, we showed that ranking of P(EAD) is qualitatively consistent with the ranking of 6 LQTS1 mutation severities according to their 30-year cardiac event rate. We then performed three studies of experimental parameter uncertainty analysis: impact of $[Ca^{2+}]_{SR}$ uncertainty on P(EB), G_{K1} uncertainty on P(EB), and LQTS1-related I_{Ks} parameter uncertainty on P(EAD). In the $[Ca^{2+}]_{SR}$ study, we discovered three patterns of P(EB) distributions: unimodal, approximately uniform, and bimodal. With increasing $[Ca^{2+}]_{SR}$ uncertainty, P(EB) uncertainty first increases and then decreases. The I_{K1} study serves as an example of using experimental uncertainty to broaden our understanding as to how a mechanistic conclusion based on experimentally measured mean behavior applies to cells with properties that deviate from the mean. In the LQTS1 study, we showed that the EU of G_{Ks} is the dominant contributor to the P(EAD) uncertainty.

Materials and Methods

Modified Walker Ventricular Myocyte Model: This study uses a modified version of the Walker et al stochastic ventricular myocyte model (10). The Walker et al. model is a biophysical-detailed three-dimensional spatial stochastic model of a cardiac ventricular myocyte containing 25,000 Ca^{2+} release sites (CRUs) (each representing a dyad) along with their sub-membrane compartments. A subset of CRUs (5400) was used for all simulations to accelerate the computation and all CRU Ca^{2+} fluxes were scaled to the total number of CRUs. This model has been shown to reproduce realistic Ca^{2+} waves as well as DADs. Chu et. al. (48) recently developed a model of the

Na^+-Ca^{2+} exchanger (NCX) that includes allosteric regulation NCX function by Ca^{2+}. This NCX model was incorporated into the Walker model. Following Chu et. al. (48), NCX was localized 15% in dyad, 30% in the submembrane compartment, and 55% in the cytosol. In addition to these changes, the time constant of Ca^{2+} flux from submembrane to cytosol was reduced by 20%, I_{Kr} conductance increased by 20%, and number of I_{to2} channels reduced from 8 to 5 in each submembrane compartment to assure a more realistic canine APD (~320 ms) and Ca^{2+} transient peak (~800 nM), similar to normal canine ventricular myocyte (49). β-adrenergic stimulation is simulated to facilitate generation of cellular arrhythmias. This was done using the β-adrenergic stimulation protocol described in Walker et. al. (10).

Long QT syndrome type 1 experiment data and I_{Ks} model.

The 17 LQTS1 clinical and experimental mutation data are obtained from Jons et. al. 2011 (8). The 30-year cardiac event rate is extracted from their Fig. 2. The 30-year cardiac event rate represents the percentage of mutation carriers that had their first cardiac event in their first 30 years of life. The focused cardiac events comprise syncope, aborted cardiac arrest, and sudden cardiac death. Clinical and experimental data from their study is summarized in Table S1. Five I_{Ks}-related parameters for each mutation are extracted from their Tables 2 and S1. In order to incorporate these five I_{Ks}-related parameters into our myocyte model, we also incorporated their I_{Ks} model in our myocyte model described by the following equations

$$
\begin{aligned}
&I_{Ks} = G_{Ks} \bullet G_{Ks}_sf \bullet \chi_{Ks} \bullet (V - E_{Ks}) \\
&\frac{d\chi_{Ks}(t)}{dt} = \frac{\chi_{Ks}(\infty) - \chi_{Ks}(t)}{\tau_{xKs}} \\
&\chi_{Ks}(\infty) = \frac{1}{1 + e^{-\frac{V - 9.4 + \Delta V_{1/2}}{11.8 \bullet k_sf}}} \\
&a_1 = 0.0000719 \frac{V}{1 + e^{-0.74V}} \bullet \frac{1}{\tau_{+}_sf} \\
&a_2 = 0.000786 \frac{V + 40}{e^{0.103(V+40)} - 1} \bullet \frac{1}{\tau_{-}_sf} \\
&\tau_{xKs} = \frac{1}{a_1 + a_2}
\end{aligned}
\qquad (1)
$$

, where τ_{+}_sf τ_{-}_sf, $\Delta V_{1/2}$, k_sf and G_{Ks}_sf are mutation-specific terms.

We selected 6 mutations (Y315C, W305S, G168R, T312I, L266P and G314S) out of 17 mutations shown in this paper. These 6 mutations cover low clinical risk to high clinical risk based on 30-year cardiac event rate.

Simulation Protocols: In the EAD studies, initial states of model state variables were the same in each simulation. These values were obtained in diastole after 10 beats during the β-adrenergic stimulation protocol. Each model simulation had a duration of 600ms. At 10ms, a 1-ms 10000 pA inward current was injected to trigger an AP. In the EB studies, the initial state of myocyte model corresponds to the diastolic state, where membrane potential is -93.4 mV, NCX is partially allosterically activated (~20%-40%), the β-adrenergic stimulation protocol is used except that RyR opening rate increases 5 times higher than in the Walker et al. model, based on experimental data for HF condition to increase the propensity for EBs (50). No external current was applied, and simulation duration was 800ms.

Statistical Modeling. Fig. 8 illustrates the general workflow for building a logistic regression model (LRM) from an underlying biophysically-detailed myocyte model. A more detailed workflow (Fig. S3) and its mathematical development is provided in the supplement. The steps of the workflow in Fig. 8 are performed twice to build the LRM. In the first iteration, relevant myocyte model inputs (MMIs), which refers collectively to myocyte model parameters as well as state variable initial conditions, and their ranges of variation (regions of interest, or ROI) are identified. ROI is established to keep MMIs within physiologically (or biophysically) relevant ranges. Multiple randomly selected MMI sets are generated by uniform sampling within these ROIs. For each sampled MMI set, multiple simulations (realizations) are performed using the Modified Walker model. A binary random variable is

defined using the output of each simulation. This random variable indicates whether the cellular arrhythmia event of interest did or did not occur. For each MMI set, an event (occurrence of an EAD or EB) probability is estimated based on its frequency of occurrence over all realizations. All MMI sets and their corresponding event probabilities are then used to derive a logistic regression model relating the probability of the event to a weighted sum of MMIs:

$$P(\text{event})=\frac{1}{1+\exp(-\underline{B}^{T}\underline{P})} \qquad (2)$$

, where $\underline{P} = \underline{P}_i$ is a vector of features, $\underline{B} = \underline{B}_i$ is a vector of weights. The subscript "*o*" stands for "initial", representing the first iteration of the pipeline. P(event) represents the estimated event occurrence probability.

After this first iteration, the logistic equation (1.2) is then used as an additional constraint to estimate the transition domain (TD) which is a subregion within the ROI for the MMI set. We then sample only within the TD in the second iteration, and steps 4 – 5 of the workflow are repeated. MMI sets and corresponding event probabilities obtained from both iterations are combined, and the final LRM is built as again using equation 1.2, where $\underline{P} = \underline{P}_f$ is the final feature vector and $\underline{B} = \underline{B}_f$ is the final weights vector. The subscript "*f*" stands for "final", representing the second iteration of the pipeline. We refer to this model as the LRM. To ensure the generalizability of the LRM, an additional 100 test MMI sets are generated within the ROI to be used for evaluation of the performance of the LRM. 100 MMI sets were generated in both the first and second iterations. For each MMI set, either 100 realizations (DAD-induced EB study) or 110 realizations (for EAD study) were simulated to estimate the probability of the event of interest. All logistic regression model fits were performed with MATLAB R2018b *fitglm* function.

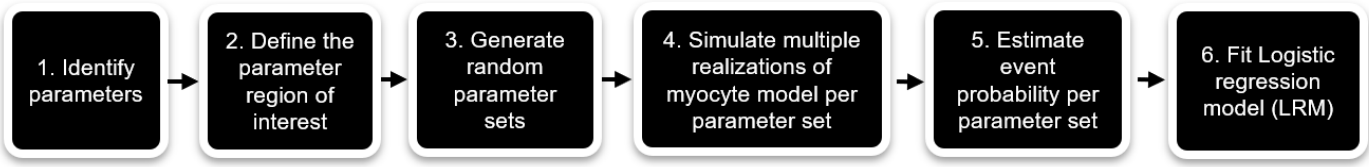

Fig. 8. General workflow pipeline for logistic model formulation

MMI Identification and MMI ROI: When building the LRM for predicting probability of occurrence of DAD-induced EBs (P(EB)), four MMIs were selected to be varied (Table 4). These were initial states of $[Ca^{2+}]_i$ and $[Ca^{2+}]_{SR}$, and scaling factors controlling I_{K1} current density (G_{K1}_sf) and RyR opening rate (k_{RyR}^{+}_sf). For simplicity, $[Ca^{2+}]_i$ and $[Ca^{2+}]_{SR}$ values mentioned in this paper all are initial state values. Upper and lower bounds on diastolic $[Ca^{2+}]_i$ and $[Ca^{2+}]_{SR}$ were obtained from experimental data (32, 51, 52). Down-regulation of I_{K1} (23) and upregulation of RyR opening rate (24) have both been shown to occur in failing heart myocytes and changes in these cellular properties are associated with cellular arrhythmias. When building the LRM for predicting probability of occurrence of EADs in the setting of LQTS1, 5 MMIs (I_{Ks}-related parameters) were selected to be varied (Table 4). These MMIs were varied over an experimentally determined range of values (± 2 standard errors) based on the work of Jons et. al.(8). Those 5 MMIs are activation time constant scaling factor (τ_+_sf), deactivation time constant scaling factor (τ_-_sf), shifting of half the maximal activation voltage ($\Delta V_{1/2}$), scaling factor of voltage dependence of activation curve slope (k_sf), and maximal conductance scaling factor (G_{Ks}_sf).

The ROI can be separated into two mutually exclusive subspaces in terms of the arrhythmia event probability: plateau domain (PD) and transition domain (TD). PD is the space where those MMI sets has P(event) from MM strictly equal 0 or 1. TD is the space where those MMI sets has P(event) from MM strictly > 0 and < 1. We can specify the Left PD (LPD) as corresponding to P(event) = 0 and the RPD as corresponding to P(event) = 1 since they are also mutually exclusive. Because of the limited number of realizations on the myocyte model for each MMI set, P(event) from MM takes on a discrete set of values so that we can strictly follow this definition.

Table 4. MMIs chosen for P(EAD) and P(EB) prediction

Event	MMIs	Lower bound	Upper bound
	τ_+_sf	0.2903	2.8510

EAD	τ_{-}_sf	0.2051	1.6577
	$\Delta V_{1/2}$	-11.9267	36.41
	k_sf	0.0000	10.8687
	G_{Ks}_sf	0.0000	1.9044
DAD-induced EB	Initial $[Ca]_i$ (nM)	100	300
	Initial $[Ca]_{SR}$ (mM)	0.3	0.7
	G_{K1}_sf	0	1
	k_{RyR}^{+}_sf	2.5	7.5

LRM Validation Metrics. Linear regression was performed between MM-generated actual P(event)s and LRM predicted P(event)s. The R-squared (R^2) from the linear regression was calculated. Absolute error between those was also calculated

$$Error = \frac{\sum_{i=1}^{n} | P_i(event)_{MM} - P_i(event)_{LRM} |}{n} \quad (3)$$

,where n is the number of MMI sets $P_i(event)_{MM}$ is event probability of ith MMI set from MM and $P_i(event)_{LRM}$ is event probability of ith MMI set from LRM.

Uncertainty Analyses: The LRM derived in this study is a function that maps MMIs to P(event). If experimental measurements of these MMIs are variable, then this variation can be modeled by assuming these measurements are drawn from an underlying probability distribution. In this case, the event probability produced by the LRM is also a random variable. We wish to characterize this uncertainty by computing the distribution of the estimated event probability. To do this, when the mean and variance of MMI estimates are available from experimental data, we assume MMIs are RVs drawn from a normal distribution with that mean and variance. To ensure the values are limited to be within a biophysically meaningful range for each MMI, distributions were truncated to exclude values outside this range. In cases where the argument of the LRM ($\underline{B}_f^T\underline{P}_f$) involves a weighted sum of individual MMIs not including quadratic features, this distribution can be calculated analytically which is the logit-normal distribution (Eq. S5) (53). In cases where the feature vector $\underline{P}_f$ includes elements containing quadratic features, P(event) has to solved numerically. In this latter case, we randomly generate (10^6) sample vectors for a specific MMI set based on the underlying MMI uncertainty distributions and use the LRM to predict P(event) for all sample vectors. In this way we could estimate the P(event) distribution.

References

1. P. F. Cranefield, R. S. Aronson, Torsade de pointes and other pause-induced ventricular tachycardias: the short-long-short sequence and early afterdepolarizations. *Pacing Clin Electrophysiol* **11**, 670-678 (1988).
2. Z. Qu, J. N. Weiss, Mechanisms of ventricular arrhythmias: from molecular fluctuations to electrical turbulence. *Annu Rev Physiol* **77**, 29-55 (2015).
3. T. Nakajima *et al.*, The mechanism of catecholaminergic polymorphic ventricular tachycardia may be triggered activity due to delayed afterdepolarization. *Eur Heart J* **18**, 530-531 (1997).
4. M. R. Rosen, Cellular electrophysiology of digitalis toxicity. *J Am Coll Cardiol* **5**, 22A-34A (1985).
5. L. S. Lilly, *Pathophysiology of heart disease: a collaborative project of medical students and faculty* (Lippincott Williams & Wilkins, 2012).
6. R. L. Winslow *et al.*, Integrative modeling of the cardiac ventricular myocyte. *Wiley Interdiscip Rev Syst Biol Med* **3**, 392-413 (2011).
7. M. Fink, P. J. Noble, D. Noble, Ca(2)(+)-induced delayed afterdepolarizations are triggered by dyadic subspace Ca2(2)(+) affirming that increasing SERCA reduces aftercontractions. *Am J Physiol Heart Circ Physiol* **301**, H921-935 (2011).
8. C. Jons *et al.*, Use of mutant-specific ion channel characteristics for risk stratification of long QT syndrome patients. *Sci Transl Med* **3**, 76ra28 (2011).
9. P. C. Yang *et al.*, In silico prediction of drug therapy in catecholaminergic polymorphic ventricular tachycardia. *The Journal of physiology* **594**, 567-593 (2016).
10. M. A. Walker, V. Gurev, J. J. Rice, J. L. Greenstein, R. L. Winslow, Estimating the probabilities of rare arrhythmic events

in multiscale computational models of cardiac cells and tissue. *PLoS Comput Biol* **13**, e1005783 (2017).
11. E. A. Sobie, Parameter sensitivity analysis in electrophysiological models using multivariable regression. *Biophys J* **96**, 1264-1274 (2009).
12. Y. S. Lee, O. Z. Liu, H. S. Hwang, B. C. Knollmann, E. A. Sobie, Parameter sensitivity analysis of stochastic models provides insights into cardiac calcium sparks. *Biophys J* **104**, 1142-1150 (2013).
13. P. J. Schwartz, L. Crotti, R. Insolia, Long-QT syndrome: from genetics to management. *Circulation: Arrhythmia and Electrophysiology* **5**, 868-877 (2012).
14. R. Hoefen *et al.*, In silico cardiac risk assessment in patients with long QT syndrome: type 1: clinical predictability of cardiac models. *Journal of the American College of Cardiology* **60**, 2182-2191 (2012).
15. I. H. T. Guideline, The non-clinical evaluation of the potential for delayed ventricular repolarization (Qt Interval Prolongation) by human pharmaceuticals. *S7B (http://www. ich. org/products/guidelines/safety/article/safety-guidelines. html)* (2005).
16. K. Blinova *et al.*, International multisite study of human-induced pluripotent stem cell-derived cardiomyocytes for drug proarrhythmic potential assessment. *Cell reports* **24**, 3582-3592 (2018).
17. M. J. Koren, M. R. Crager, M. Sweeney, Long-term safety of a novel antianginal agent in patients with severe chronic stable angina: the Ranolazine Open Label Experience (ROLE). *Journal of the American College of Cardiology* **49**, 1027-1034 (2007).
18. B. R. Chaitman *et al.*, Effects of ranolazine with atenolol, amlodipine, or diltiazem on exercise tolerance and angina frequency in patients with severe chronic angina: a randomized controlled trial. *Jama* **291**, 309-316 (2004).
19. S. Tzeis, G. Andrikopoulos, Antiarrhythmic properties of ranolazine–from bench to bedside. *Expert opinion on investigational drugs* **21**, 1733-1741 (2012).
20. J. Paavola *et al.*, Mutant ryanodine receptors in catecholaminergic polymorphic ventricular tachycardia generate delayed afterdepolarizations due to increased propensity to Ca2+ waves. *European heart journal* **28**, 1135-1142 (2007).
21. N. M. Plaster *et al.*, Mutations in Kir2.1 cause the developmental and episodic electrical phenotypes of Andersen's syndrome. *Cell* **105**, 511-519 (2001).
22. A. A. Domenighetti, C. Boixel, D. Cefai, H. Abriel, T. Pedrazzini, Chronic angiotensin II stimulation in the heart produces an acquired long QT syndrome associated with IK1 potassium current downregulation. *Journal of molecular and cellular cardiology* **42**, 63-70 (2007).
23. S. M. Pogwizd, K. Schlotthauer, L. Li, W. Yuan, D. M. Bers, Arrhythmogenesis and contractile dysfunction in heart failure: roles of sodium-calcium exchange, inward rectifier potassium current, and residual β-adrenergic responsiveness. *Circulation research* **88**, 1159-1167 (2001).
24. Z. Kubalova *et al.*, Abnormal intrastore calcium signaling in chronic heart failure. *Proceedings of the National Academy of Sciences* **102**, 14104-14109 (2005).
25. I. Mikuni, C. G. Torres, M. W. Bienengraeber, W.-M. Kwok, Partial restoration of the long QT syndrome associated KCNQ1 A341V mutant by the KCNE1 β-subunit. *Biochimica et Biophysica Acta (BBA)-General Subjects* **1810**, 1285-1293 (2011).
26. Q. Wang *et al.*, Positional cloning of a novel potassium channel gene: KVLQT1 mutations cause cardiac arrhythmias. *Nat Genet* **12**, 17-23 (1996).
27. JCGM (2008) Joint Committee for Guides in Metrology. (Bureau International des Poids et Mesures Sèvres, France).
28. S. Marino, I. B. Hogue, C. J. Ray, D. E. Kirschner, A methodology for performing global uncertainty and sensitivity analysis in systems biology. *Journal of theoretical biology* **254**, 178-196 (2008).
29. R. H. Johnstone *et al.*, Uncertainty and variability in models of the cardiac action potential: Can we build trustworthy models? *Journal of molecular and cellular cardiology* **96**, 49-62 (2016).
30. O. J. Britton *et al.*, Experimentally calibrated population of models predicts and explains intersubject variability in cardiac cellular electrophysiology. *Proceedings of the National Academy of Sciences* **110**, E2098-E2105 (2013).
31. E. Bovo, S. R. Mazurek, L. A. Blatter, A. V. Zima, Regulation of sarcoplasmic reticulum Ca2+ leak by cytosolic Ca2+ in rabbit ventricular myocytes. *The Journal of physiology* **589**, 6039-6050 (2011).
32. T. R. Shannon, K. S. Ginsburg, D. M. Bers, Quantitative assessment of the SR Ca2+ leak-load relationship. *Circulation*

research **91**, 594-600 (2002).
33. A. V. Zima, E. Bovo, D. M. Bers, L. A. Blatter, Ca2+ spark-dependent and-independent sarcoplasmic reticulum Ca2+ leak in normal and failing rabbit ventricular myocytes. *The Journal of physiology* **588**, 4743-4757 (2010).
34. P. J. Schwartz *et al.*, Genotype-phenotype correlation in the long-QT syndrome: gene-specific triggers for life-threatening arrhythmias. *Circulation* **103**, 89-95 (2001).
35. T. Liu, D. A. Brown, B. O'Rourke, Role of mitochondrial dysfunction in cardiac glycoside toxicity. *Journal of molecular and cellular cardiology* **49**, 728-736 (2010).
36. A. S. Dhamoon, J. Jalife, The inward rectifier current (IK1) controls cardiac excitability and is involved in arrhythmogenesis. *Heart Rhythm* **2**, 316-324 (2005).
37. D. Bers, *Excitation-contraction coupling and cardiac contractile force* (Springer Science & Business Media, 2001), vol. 237.
38. T. R. Chay, Y. S. Lee, Studies on re-entrant arrhythmias and ectopic beats in excitable tissues by bifurcation analyses. *J Theor Biol* **155**, 137-171 (1992).
39. D. X. Tran *et al.*, Bifurcation and chaos in a model of cardiac early afterdepolarizations. *Phys Rev Lett* **102**, 258103 (2009).
40. P. Kugler, Early Afterdepolarizations with Growing Amplitudes via Delayed Subcritical Hopf Bifurcations and Unstable Manifolds of Saddle Foci in Cardiac Action Potential Dynamics. *PLoS One* **11**, e0151178 (2016).
41. T. Nagano *et al.*, Single-cell Hi-C reveals cell-to-cell variability in chromosome structure. *Nature* **502**, 59 (2013).
42. A. Amantonico, P. L. Urban, S. R. Fagerer, R. M. Balabin, R. Zenobi, Single-cell MALDI-MS as an analytical tool for studying intrapopulation metabolic heterogeneity of unicellular organisms. *Analytical chemistry* **82**, 7394-7400 (2010).
43. A. E. Lacerda *et al.*, Alfuzosin delays cardiac repolarization by a novel mechanism. *Journal of Pharmacology and Experimental Therapeutics* **324**, 427-433 (2008).
44. F. G. Akar *et al.*, Phenotypic differences in transient outward K+ current of human and canine ventricular myocytes: insights into molecular composition of ventricular Ito. *Am J Physiol Heart Circ Physiol* **286**, H602-609 (2004).
45. Y. Xie, D. Sato, A. Garfinkel, Z. Qu, J. N. Weiss, So little source, so much sink: requirements for afterdepolarizations to propagate in tissue. *Biophysical journal* **99**, 1408-1415 (2010).
46. J. Eldstrom, Z. Wang, D. Werry, N. Wong, D. Fedida, Microscopic mechanisms for long QT syndrome type 1 revealed by single-channel analysis of IKs with S3 domain mutations in KCNQ1. *Heart Rhythm* **12**, 386-394 (2015).
47. C. L. Anderson *et al.*, Most LQT2 mutations reduce Kv11.1 (hERG) current by a class 2 (trafficking-deficient) mechanism. *Circulation* **113**, 365-373 (2006).
48. L. Chu, J. L. Greenstein, R. L. Winslow, Modeling Na(+)-Ca(2+) exchange in the heart: Allosteric activation, spatial localization, sparks and excitation-contraction coupling. *J Mol Cell Cardiol* **99**, 174-187 (2016).
49. B. O'Rourke *et al.*, Mechanisms of altered excitation-contraction coupling in canine tachycardia-induced heart failure, I: experimental studies. *Circ Res* **84**, 562-570 (1999).
50. Z. Kubalova *et al.*, Abnormal intrastore calcium signaling in chronic heart failure. *Proc Natl Acad Sci U S A* **102**, 14104-14109 (2005).
51. D. J. Beuckelmann, M. Näbauer, E. Erdmann, Intracellular calcium handling in isolated ventricular myocytes from patients with terminal heart failure. *Circulation* **85**, 1046-1055 (1992).
52. J. Curran *et al.*, Nitric oxide-dependent activation of CaMKII increases diastolic sarcoplasmic reticulum calcium release in cardiac myocytes in response to adrenergic stimulation. *PloS one* **9**, e87495 (2014).
53. J. Atchison, S. M. Shen, Logistic-normal distributions: Some properties and uses. *Biometrika* **67**, 261-272 (1980).